the notion that the regulation of *Tert* by β-catenin is a general biological feature. Our mouse model (villin-creERT × β-cat$^{Ex3fl/+}$) provides in vivo evidence that the aberrant activation of β-catenin in the epithelium of the small intestine leads to *Tert* expression and binding of β-catenin to the *Tert* promoter. Exon 3 encodes phosphorylation sites important for β-catenin protein stability (*14*), and these sites are frequently mutated in human colorectal and other cancers (*15*). It is notable that in human colorectal cancers, high *Tert* and β-catenin expression are significantly correlated ($P = 0.0001$), as taken from publicly available microarray data sets (*16*) (Fig. 5F and fig. S11A).

Conclusion. By identifying *Tert* as a target gene of β-catenin, we demonstrate a link between these two key regulators in stem cell biology and cancer. From the results presented here, we propose that mutations in β-catenin can lead to an enhanced *Tert* expression in human cancer, which results in the stabilization of telomeres, one of the hallmarks of tumorigenesis.

References and Notes

1. M. A. Blasco, *Nat. Rev. Genet.* **8**, 299 (2007).
2. H. D. Wyatt, S. C. West, T. L. Beattie, *Nucleic Acids Res.* **38**, 5609 (2010).
3. T. Miura, M. P. Mattson, M. S. Rao, *Aging Cell* **3**, 333 (2004).
4. S. Y. Sokol, *Development* **138**, 4341 (2011).
5. T. Reya, H. Clevers, *Nature* **434**, 843 (2005).
6. V. F. Taelman *et al.*, *Cell* **143**, 1136 (2010).
7. C. W. Wong *et al.*, *Stem Cells* **28**, 1510 (2010).
8. B. Schuettengruber, A. M. Martinez, N. Iovino, G. Cavalli, *Nat. Rev. Mol. Cell Biol.* **12**, 799 (2011).
9. T. Sato *et al.*, *Nature* **459**, 262 (2009).
10. O. Basak, V. Taylor, *Eur. J. Neurosci.* **25**, 1006 (2007).
11. N. Harada *et al.*, *EMBO J.* **18**, 5931 (1999).
12. J. I. Park *et al.*, *Nature* **460**, 66 (2009).
13. C. Mosimann, G. Hausmann, K. Basler, *Nat. Rev. Mol. Cell Biol.* **10**, 276 (2009).
14. H. Aberle, A. Bauer, J. Stappert, A. Kispert, R. Kemler, *EMBO J.* **16**, 3797 (1997).
15. V. Korinek *et al.*, *Science* **275**, 1784 (1997).
16. S. Kaiser *et al.*, *Genome Biol.* **8**, R131 (2007).

Acknowledgments: We thank H. H. Ng (Singapore) for the antibody against Klf4, I. Horikawa (NIH) for the 300-bp promoter construct, and J.-H. Lee (Indiana University) for Ash2l and Setd1a expression vectors. We thank E. M. Varela and M. Blasco (Madrid) for advice and reagents for the Q-fish analysis and for antibodies against Tert. We are grateful to M. M. Taketo (Kyoto) and to S. Robine (Paris) for providing mutant mice. We thank S. Lugert for advice on neurosphere cultures, J. Volkind for technical assistance, V. Taylor and D. Junghans for discussion and critical reading, and R. Schneider for typing of the manuscript. K.H. and A.R. are members of the International Max Planck Research School for Molecular and Cellular Biology (IMPRS-MCB). This work was supported by the Max Planck Society. The authors declare no financial interests.

Supplementary Materials

www.sciencemag.org/cgi/content/full/336/6088/1549/DC1
Materials and Methods
Figs. S1 to S11
Tables S1 to S3
References (*17*–*25*)

22 December 2011; accepted 9 April 2012
10.1126/science.1218370

REPORTS

A Sharp Peak of the Zero-Temperature Penetration Depth at Optimal Composition in $BaFe_2(As_{1-x}P_x)_2$

K. Hashimoto,[1]* K. Cho,[2,3] T. Shibauchi,[1]† S. Kasahara,[1,4] Y. Mizukami,[1] R. Katsumata,[1] Y. Tsuruhara,[1] T. Terashima,[4] H. Ikeda,[1] M. A. Tanatar,[2] H. Kitano,[5] N. Salovich,[6] R. W. Giannetta,[6] P. Walmsley,[7] A. Carrington,[7] R. Prozorov,[2,3] Y. Matsuda[1]†

In a superconductor, the ratio of the carrier density, n, to its effective mass, m^*, is a fundamental property directly reflecting the length scale of the superfluid flow, the London penetration depth, λ_L. In two-dimensional systems, this ratio n/m^* ($\sim 1/\lambda_L^2$) determines the effective Fermi temperature, T_F. We report a sharp peak in the x-dependence of λ_L at zero temperature in clean samples of $BaFe_2(As_{1-x}P_x)_2$ at the optimum composition $x = 0.30$, where the superconducting transition temperature T_c reaches a maximum of 30 kelvin. This structure may arise from quantum fluctuations associated with a quantum critical point. The ratio of T_c/T_F at $x = 0.30$ is enhanced, implying a possible crossover toward the Bose-Einstein condensate limit driven by quantum criticality.

In two families of high-temperature superconductors, cuprates and iron-pnictides, superconductivity emerges in close proximity to an antiferromagnetically ordered state, and the critical temperature, T_c, has a dome-shaped dependence on doping or pressure (*1*–*3*). What happens inside this superconducting dome is still a matter of debate (*3*–*5*). In particular, elucidating whether a quantum critical point (QCP) is hidden inside it (Fig. 1, A and B) may be key to understanding high-T_c superconductivity (*5*, *6*). A QCP marks the position of a quantum phase transition (QPT), a zero-temperature phase transition driven by quantum fluctuations (*7*).

The London penetration depth, λ_L, is a property that may be measured at low temperature in the superconducting state to probe the electronic structure of the material and to look for signatures of a QCP. The absolute value of λ_L in the zero-temperature limit immediately gives the superfluid density $\lambda_L^{-2}(0) = \mu_0 e^2 \Sigma_i n_i/m_i^*$, which is a direct probe of the superconducting state; here, m_i^* and n_i are the effective mass and concentration of the superconducting carriers in band i, respectively (*8*). Measurements on high-quality crystals are necessary because impurities and inhomogeneity may otherwise wipe out the signatures of the QPT. Another advantage of this approach is that it does not require the application of a strong magnetic field, which may induce a different QCP or shift the zero-field QCP (*9*).

$BaFe_2(As_{1-x}P_x)_2$ is a particularly suitable system for penetration depth measurements because, in contrast to most other Fe-based superconductors, very clean (*10*) and homogeneous crystals of the whole composition series can be grown (*11*). In this system, the isovalent substitution of P for As in the parent compound $BaFe_2As_2$ offers an elegant way to suppress magnetism and induce superconductivity (*11*). Non–Fermi liquid properties are apparent in the normal state above the superconducting dome (Fig. 2A) (*11*, *12*), and de Haas–van Alphen (dHvA) oscillations (*10*) have been observed over a wide x range, including the superconducting compositions, giving detailed information on the electronic structure. Because P and As are isoelectronic, the system remains compensated for all values of x (i.e., volumes of the electron and hole Fermi surfaces are equal).

As discussed in (*10*), the normal-state electronic structure of $BaFe_2(As_{1-x}P_x)_2$ determined by dHvA experiments is significantly modified from that predicted by conventional density functional theory (DFT) band structure calculations. Figure 2A shows the composition evolution of the effective mass, m^*, normalized by the free

[1]Department of Physics, Kyoto University, Kyoto 606-8502, Japan. [2]The Ames Laboratory, Ames, IA 5001, USA. [3]Department of Physics and Astronomy, Iowa State University, Ames, IA 50011, USA. [4]Research Center for Low Temperature and Materials Sciences, Kyoto University, Kyoto 606-8501, Japan. [5]Department of Physics and Mathematics, Aoyama Gakuin University, 5-10-1 Fuchinobe, Chuo-ku, Sagamihara, Kanagawa 252-5258, Japan. [6]Loomis Laboratory of Physics, University of Illinois at Urbana-Champaign, 1110 West Green Street, Urbana, IL 61801, USA. [7]H. H. Wills Physics Laboratory, University of Bristol, Tyndall Avenue, Bristol, UK.

*Present address: Institute for Materials Research, Tohoku University, Sendai 980-8577, Japan.
†To whom correspondence should be addressed. E-mail: matsuda@scphys.kyoto-u.ac.jp (Y.M.); shibauchi@scphys.kyoto-u.ac.jp (T.S.)

electron mass, m_0, and the Fermi temperature, $T_F = \varepsilon_F/k_B = \frac{\hbar e^2}{2\pi k_B m^*} A_k$, for $x > 0.4$, determined from the dHvA oscillations corresponding to the extremal orbits on the outer electron Fermi surface (β_1 and β_2 orbits in Fig. 2B). Here, ε_F is the Fermi energy and A_k is the cross-sectional area of the orbit. In contrast to the negligible x-dependence expected from the DFT calculations, a critical-like increase in m^* accompanied by a strong reduction of T_F is observed as the system is tuned toward the optimal composition from the overdoped side.

For a reliable determination of the absolute value of $\lambda_L(0)$ in small single crystals, we adopted three different methods (*8*). The first is the lower-T_c superconducting film coating method (*13*–*15*), in which $\lambda_L(0)$ is determined from the frequency shift of a high-precision tunnel diode oscillator (*16*) (resonant frequency of $f \sim 13$ MHz) containing the $BaFe_2(As_{1-x}P_x)_2$ crystal coated with an aluminum film ($T_c = 1.2$ K) of known thickness and penetration depth.

The second is the microwave cavity perturbation technique, in which $\lambda_L(0)$ is determined from the measurements of surface impedance, $Z_s = R_s + iX_s$, by using a superconducting resonator ($f \sim 28$ GHz) and a rutile cavity resonator ($f \sim 5$ GHz), both of which have a very high quality factor $Q \sim 10^6$ (*8*). In all crystals, the residual surface resistance $R_s(0)$ at $T \to 0$ K, which we determined by withdrawing the crystal from the rutile cavity at low temperature, is less than 0.3% of R_s just above T_c. This negligible residual $R_s(0)$ indicates almost perfect Meissner screening without any non-superconducting regions. In the superconducting state well below T_c, $\lambda_L(T)$ is obtained from the surface reactance via the relation $X_s(T) = \mu_0\omega\lambda_L(T)$. The absolute value of X_s is determined from Z_s and dc-resistivity ρ_{dc} (measured separately by a conventional four contact technique) by the relation $R_s = X_s = \sqrt{\mu_0\omega\rho_{dc}/2}$ which holds in the normal state (*8*).

The third method uses the temperature-dependent changes $\delta\lambda_L(T) = \lambda_L(T) - \lambda_L(0)$, measured by the tunnel diode oscillator down

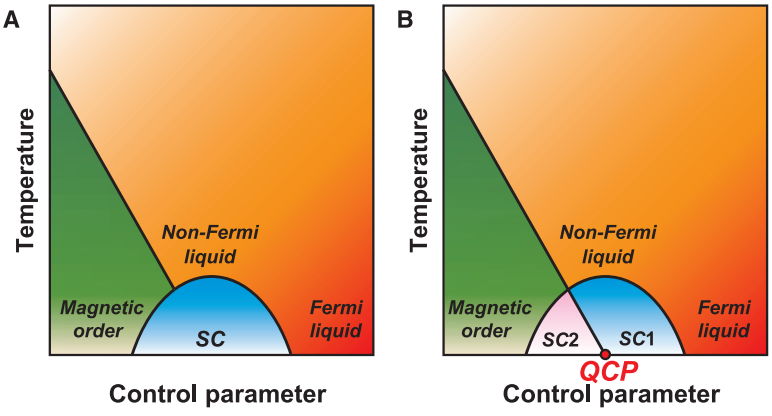

Fig. 1. Generic temperature versus nonthermal control parameter phase diagram of iron-based superconductors, illustrating two cases. (**A**) Quantum criticality is avoided by the transition to the superconducting state. There is only one superconducting phase. (**B**) A QCP lies beneath the superconducting dome. The QCP separates two distinct superconducting phases (SC1 and SC2). In the case of (A), non–Fermi liquid behavior may appear above the dome if there is a QCP located along the axis of another control parameter that is independent of the control parameter shown on the abscissa. In the case of (B), non–Fermi liquid behavior appears because of the QCP inside the dome.

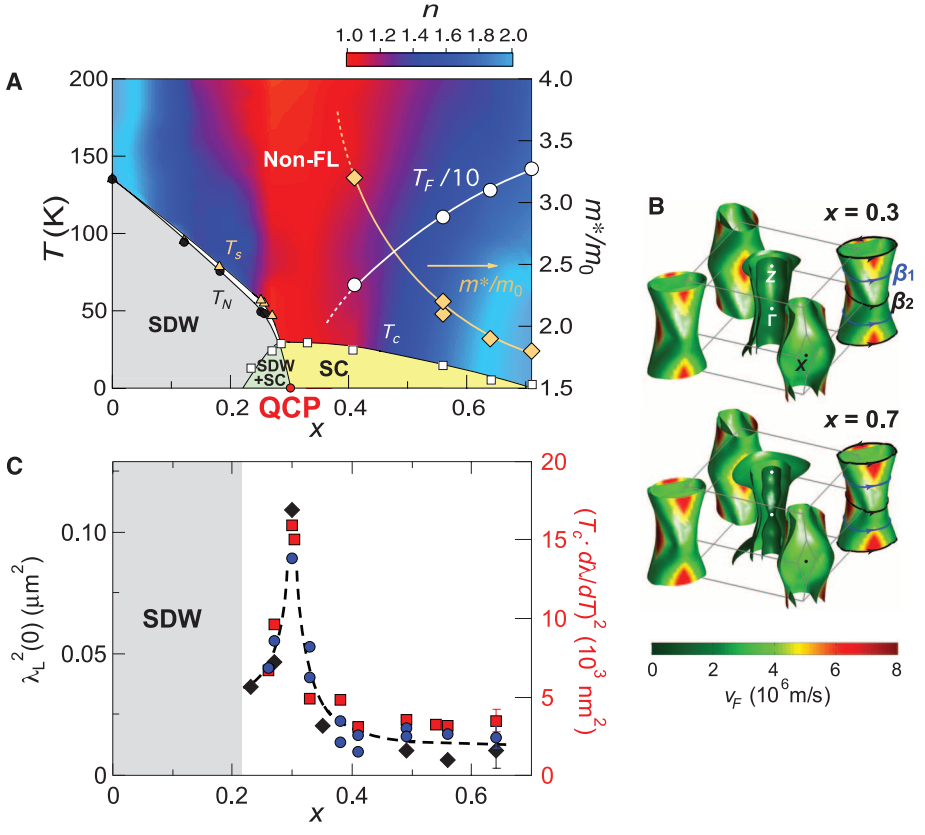

Fig. 2. (**A**) Phase diagram of $BaFe_2(As_{1-x}P_x)_2$. The transition to the SDW ground state at T_N coincides with or is preceded by the structural transition at T_s. With increasing x, T_N decreases and goes to zero continuously at $x = 0.30$. The superconducting dome extends over a composition range $0.22 < x < 0.7$, with maximum $T_c = 30$ K at $x = 0.30$. The red shaded region at around $x = 0.30$ represents the region where the exponent n of the temperature dependence of the resistivity, $\rho_{dc}(T) = \rho(0) + aT^n$, is close to unity, which is a hallmark of a non-Fermi liquid (non-FL). The composition dependence of the effective Fermi temperature T_F and renormalized mass m^*/m_0 determined by dHvA oscillations (*10*) arising from the β orbits [shown in (B)] are also plotted. (**B**) Fermi surface of $BaFe_2(As_{1-x}P_x)_2$ with $x = 0.3$ and 0.7 from the band-structure calculation using DFT as implemented in the WIEN2K code (*10*). The Fermi surface consists of five quasi-cylindrical pockets, three hole pockets at the center of the Brillouin zone, and two electron pockets centered at its corners. The shading represents the in-plane Fermi velocity, v_F. The flat parts of the outer electron sheets have high v_F values. The lines represent the extremal β orbits. (**C**) Composition evolution of the square of the London penetration depth $\lambda_L^2(0)$ in the zero-temperature limit determined by three different methods: aluminum coating method (black diamonds), microwave cavity perturbation technique (blue circles), and the low-temperature slope of the change of the penetration depth with temperature (red squares, right-hand scale) shown in Fig. 3. Different points for the same x correspond to different crystals from the same batch, but for some of the microwave and the low-temperature slope data we used the same crystals. Error bars shown for $x = 0.64$ represent typical experimental errors (*8*) largely resulting from uncertainties in the determination of geometrical factors.

to ~ 80 mK (Fig. 3). For all samples measured, covering a wide range of concentrations $0.26 \leq x \leq 0.64$, a quasi–T-linear variation of $\delta\lambda_L(T)$ is observed. This important result indicates that the presence of line nodes in the superconducting gap (*16*) is a robust feature of this P-substituted system. This robustness is consistent with the nodes being on the electron sheets (*17*) rather than the hole sheets, because the electron sheets change relatively little with x whereas the shape of the hole sheets changes substantially (Fig. 2B). A notable feature of the T-linear penetration depth is that the relative slope $d\lambda_L/d(T/T_c)$ is steepest for $x = 0.30$ (Fig. 3B). In general, this slope is determined by the Fermi velocity and the $\boldsymbol{k}$ dependence of the superconducting gap close to the node. Making the reasonable assumption that the gap structure evolves weakly across the phase diagram, the x dependence of $d\lambda_L/d(T/T_c)$ will mirror that of $\lambda_L(0)$ (*8*).

Figure 2C shows the composition dependence of the squared in-plane London penetration length $\lambda_L^{-2}(0)$ in the zero-temperature limit. Although different techniques can involve systematic errors (*15*), all three methods give very similar x dependencies. The most notable feature is the sharp peak in $\lambda_L^{-2}(0)$ at $x = 0.30$, at about the same composition level where T_c is maximal. The prominent enhancement of $\lambda_L^{-2}(0)$ is observed on approaching $x = 0.30$ from either side and has been seen in multiple samples by using different techniques. This reproducibility, combined with the above mentioned low $R_s(0)$, sharp superconducting transitions, and large heat capacity anomalies at all values of x close to $x = 0.30$ (*8*), shows that the enhancement is not an experimental artifact associated with poor screening caused by nonbulk superconductivity. We attribute the peak in $\lambda_L^{-2}(0)$ to the existence of a QCP at $x = 0.30$.

This result contrasts with the behavior found for the electron-doped iron-based superconductors, $Ba(Fe_{1-x}Co_x)_2As_2$, where a shallow minimum of $\lambda_L(0)$ at the optimum doping and a continuous increase on the underdoped side have been reported (*14*, *15*, *21*). This difference from the present case may be related to a greater degree of electronic disorder in the Fe layer caused by the Co doping (*1*, *2*), which may smear out the singularity. The difference in the superconducting gap structure (*2*) as well as the addition of charge carriers from the Co doping may also be a source of differences in the x-dependence of $\lambda_L(0)$.

In cuprates, a QCP associated with the pseudogap formation has been suggested to occur at the hole concentration $p \sim 0.19$ inside the superconducting dome. However, there does not appear to be any evidence of mass divergence at this purported QCP, and at this doping a broad minimum of $\lambda_L^{-2}(0)$ was reported (*22*). An enhancement in $\lambda_L^{-2}(0)$ has been observed at $p \sim 1/8$ (*23*), but this is accompanied by a reduction of T_c, which is again different from the present case where the peak in $\lambda_L^{-2}(0)$ coincides with the maximum T_c.

Our results may have general implications for the behavior of $\lambda_L^{-2}(0)$ in strongly correlated superconducting systems. How strong electron correlations influence the condensed electron pairs in superconductors has been a long-standing issue (*24*–*26*). In fact, it has been pointed out that, in an ordinary one-component Galilean invariant Fermi liquid, electron correlation effects do not cause the renormalization of λ_L in the superconducting state (*24*). However, experimentally

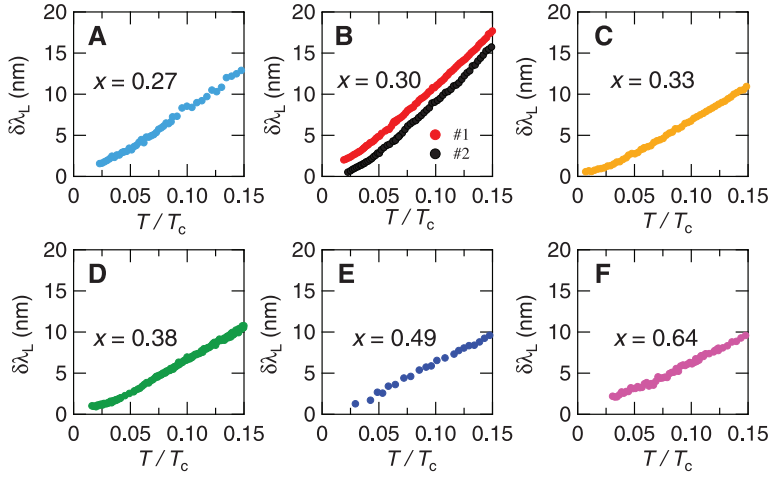

Fig. 3. Relative change of the penetration depth, $\delta\lambda_L(T) = \lambda_L(T) - \lambda_L(0)$, at low temperatures plotted against T/T_c for different compositions from $x = 0.27$ (**A**) to 0.64 (**F**). For $x = 0.30$, data for two samples are shown, one of which (#2) is shifted vertically for clarity.

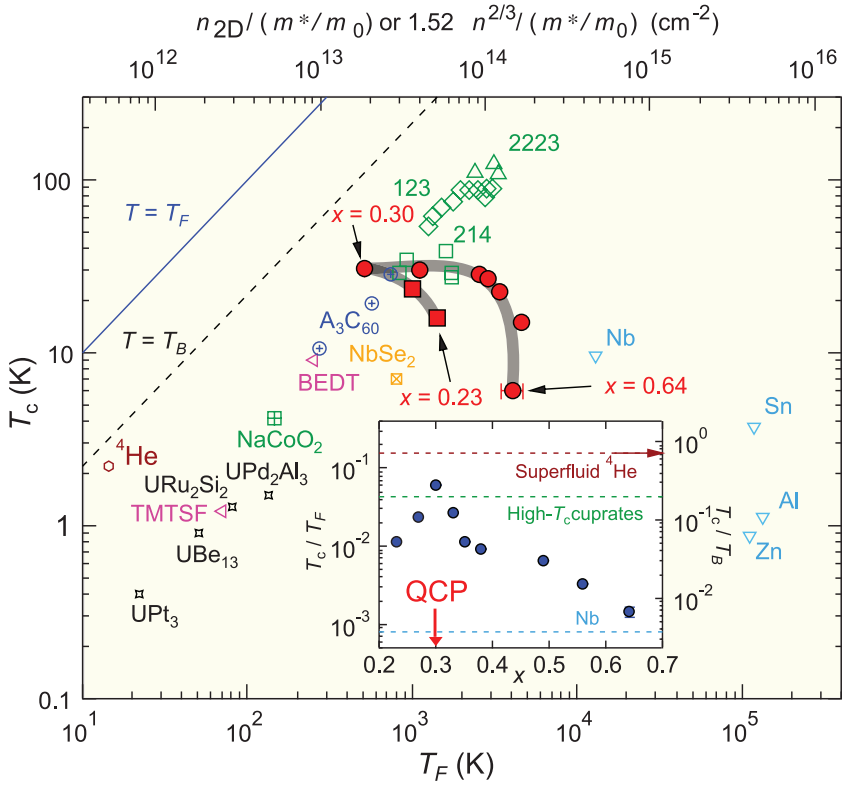

Fig. 4. Uemura plot. T_c is plotted as a function of T_F evaluated from $1/\lambda_L^{-2}(0)$ for various superconductors [$n_{2D}/(m^*/m_0)$ for 2D and $1.52n^{2/3}/(m^*/m_0)$ for 3D systems] (*27*). We used an average of the Al-coating and microwave data for $BaFe_2(As_{1-x}P_x)_2$. The data for $x \geq 0.30$ (red circles) and for $x < 0.30$ (red squares) bridge a gap between the conventional superconductors such as Nb and cuprate high-T_c superconductors such as $(La,Sr)_2CuO_4$ (214), $YBa_2Cu_3O_{7-\delta}$ (123), and $Bi_2Sr_2Ca_2Cu_3O_y$ (2223). $x = 0.30$ represents the data at the QCP. The dashed line is the BEC temperature for the ideal 3D boson gas. (**Inset**) Composition dependence of T_c normalized by the Fermi temperature (left axis) or BEC temperature (right axis). Green and light blue dashed lines mark the T_c/T_F values for underdoped cuprates 123 and for the conventional superconductor Nb. Brown arrow represents $T_c/T_B = 0.7$ for superfluid ^{4}He.

$\lambda_L^{-2}(0)$ does appear to be enhanced in heavy-fermion superconductors, which contain interacting conduction electrons and local moments (*25*, *26*). The present results in $BaFe_2(As_{1-x}P_x)_2$ support this and suggest that in sufficiently clean systems electron correlation effects can lead to a striking renormalization of $\lambda_L^{-2}(0)$.

We now discuss the consequences of a QPT inside the superconducting dome. Such a QPT implies that the non–Fermi liquid behavior indicated by the red region in Fig. 2A is most likely associated with a finite temperature quantum critical region linked to the QCP. Moreover, this transition immediately indicates two distinct superconducting ground states. In our system, the robust T-linear behavior of $\delta\lambda_L(T)$ on both sides of the purported QCP at $x = 0.30$ argues against a drastic change in the superconducting gap structure (*2*, *6*). The fact that the zero-temperature extrapolation of the antiferromagnetic transition $T_N(x)$ into the dome (*12*) coincides with the location of the QCP (Fig. 2A) may indicate that the QCP separates a pure superconducting phase on the right and a superconducting phase coexisting with spin-density-wave (SDW) order on the left (Fig. 1B).

To place $BaFe_2(As_{1-x}P_x)_2$ in the context of other superconductors, we plotted T_c as a function of the effective Fermi temperature T_F for several types of compounds (Uemura plot, Fig. 4); the red symbols correspond to various values of x for $BaFe_2(As_{1-x}P_x)_2$ studied here, and the others are obtained from μSR measurements reported previously (*27*). Because the relevant Fermi surface sheets are nearly cylindrical, T_F for two-dimensional (2D) systems may be estimated directly from $\lambda_L(0)$ via the relation $T_F = \frac{(\hbar^2\pi)n_{2D}}{k_B m^*} \approx \left(\frac{\hbar^2\pi}{\mu_0 e^2 d}\right)\lambda_L^{-2}(0)$, where n_{2D} is the carrier concentration within the superconducting planes and d is the interlayer spacing; $T_F = (\hbar^2/2)(3\pi^2)^{2/3}n^{2/3}/k_B m^*$ for 3D systems (*27*). The dashed line corresponds to the Bose-Einstein condensation (BEC) temperature for an ideal 3D boson gas, $T_B = \frac{\hbar^2}{2\pi m^* k_B}\left(\frac{n}{2.612}\right)^{2/3}$. In a quasi-2D system, this value of T_B provides an estimate of the maximum condensate temperature. The evolution of T_c with T_F in the present system is in sharp contrast to that in cuprates, in which T_c is roughly scaled by T_F. The inset of Fig. 4 depicts the x-composition dependence of T_c normalized by Fermi (or BEC) temperature, T_c/T_F (T_c/T_B). In the large composition region ($x > 0.6$), T_c/T_F is very small, comparable to that of the conventional superconductor Nb. As x is decreased, T_c/T_F increases rapidly and then decreases in the SDW region after reaching the maximum at the QCP ($x = 0.30$). Notably, the magnitude of T_c/T_B (≈0.30) at the QCP exceeds that of cuprates and reaches almost 40% of the value of superfluid ^{4}He.

The fact that T_c/T_F becomes largest at the QCP indicates that the strongest pairing interaction is achieved at the QCP, implying that high-T_c superconductivity is driven by the QCP. In a multiband system, we need to introduce the effective Fermi energy ε_F for each band, which is defined for electron bands as the energy of the highest occupied state relative to the top of the band and for hole bands as the energy of the highest occupied state relative to the bottom of the band. Because the outer electron sheet with the highest Fermi velocity has the largest ε_F and hence the largest contribution to $\lambda_L^{-2}(0)$, the magnitudes of T_c/T_F in the other sheets are expected to be even larger. These results lead us to consider that in terms of T_c/T_F the system is closer to the Bardeen-Cooper-Schrieffer–BEC crossover (*28*–*30*) than the cuprates.

References and Notes

1. G. R. Stewart, *Rev. Mod. Phys.* **83**, 1589 (2011).
2. P. J. Hirschfeld, M. M. Korshunov, I. I. Mazin, *Rep. Prog. Phys.* **74**, 124508 (2011).
3. M. R. Norman, D. Pines, C. Kallin, *Adv. Phys.* **54**, 715 (2005).
4. J. Dai, Q. Si, J.-X. Zhu, E. Abrahams, *Proc. Natl. Acad. Sci. U.S.A.* **106**, 4118 (2009).
5. D. M. Broun, *Nat. Phys.* **4**, 170 (2008).
6. R. M. Fernandes, J. Schmalian, *Phys. Rev. B* **82**, 014521 (2010).
7. See, for example, S. Sachdev, B. Keimer, *Phys. Today* **64**, 29 (2011).
8. See supplementary materials on *Science* Online.
9. E. G. Moon, S. Sachdev, *Phys. Rev. B* **80**, 035117 (2009).
10. H. Shishido *et al.*, *Phys. Rev. Lett.* **104**, 057008 (2010).
11. S. Kasahara *et al.*, *Phys. Rev. B* **81**, 184519 (2010).
12. Y. Nakai *et al.*, *Phys. Rev. Lett.* **105**, 107003 (2010).
13. R. Prozorov, R. W. Giannetta, *Supercond. Sci. Technol.* **19**, R41 (2006).
14. R. T. Gordon *et al.*, *Phys. Rev. B* **82**, 054507 (2010).
15. R. Prozorov, V. G. Kogan, *Rep. Prog. Phys.* **74**, 124505 (2011).
16. K. Hashimoto *et al.*, *Phys. Rev. B* **81**, 220501(R) (2010).
17. M. Yamashita *et al.*, *Phys. Rev. B* **84**, 060507(R) (2011).
18. C. Chaparro *et al.*, Doping dependence of the specific heat of single crystal $BaFe_2(As_{1-x}P_x)_2$ (2011); http://arxiv.org/abs/1110.3075.
19. S. L. Bud'ko, N. Ni, P. C. Canfield, *Phys. Rev. B* **79**, 220516(R) (2009).
20. J. Zaanen, *Phys. Rev. B* **80**, 212502 (2009).
21. L. Luan *et al.*, *Phys. Rev. Lett.* **106**, 067001 (2011).
22. J. L. Tallon, J. W. Loram, J. R. Cooper, C. Panagopoulos, C. Bernhard, *Phys. Rev. B* **68**, 180501 (2003).
23. C. Panagopoulos *et al.*, *Phys. Rev. B* **66**, 064501 (2002).
24. A. J. Leggett, *Phys. Rev.* **140**, A1869 (1965).
25. C. M. Varma, K. Miyake, S. Schmitt-Rink, *Phys. Rev. Lett.* **57**, 626 (1986).
26. F. Gross *et al.*, *Z. Phys. B* **64**, 175 (1986).
27. Y. J. Uemura, *J. Phys. Condens. Matter* **16**, S4515 (2004).
28. Q. Chen, J. Stajic, S. Tan, K. Levin, *Phys. Rep.* **412**, 1 (2005).
29. C. Sá de Melo, M. Randeria, J. R. Engelbrecht, *Phys. Rev. Lett.* **71**, 3202 (1993).
30. Y. J. Uemura, *Physica B* **404**, 3195 (2009).

Acknowledgments: We thank R. M. Fernandes, S. Kivelson, H. Kontani, Q. Si, U. Welp, and Y. Yanase for valuable discussion. Supported by Grant-in-Aid for the Global Centers of Excellence program "The Next Generation of Physics, Spun from Universality and Emergence," Grant-in-Aid for Scientific Research on Innovative Areas "Heavy Electrons" from the Ministry of Education, Culture, Sports, Science and Technology of Japan, KAKENHI from Japan Society for the Promotion of Science, and the Engineering and Physical Sciences Research Council (UK). Work at the Ames Laboratory was supported by the U.S. Department of Energy, Basic Energy Sciences, Materials Science and Engineering Division, under contract no. DE-AC02-07CH11358. Work at the University of Illinois was supported by the Center for Emergent Superconductivity, an Energy Frontier Research Center funded by the U.S. Department of Energy, Office of Science, Office of Basic Energy Sciences under award no. DE-AC0298CH1088.

Supplementary Materials

www.sciencemag.org/cgi/content/full/336/6088/1554/DC1
Materials and Methods
Supplementary Text
Figs. S1 to S5
References (*31*–*42*)

30 January 2012; accepted 10 May 2012
10.1126/science.1219821

Electromechanical Properties of Graphene Drumheads

Nikolai N. Klimov,[1,2,3] Suyong Jung,[1,2]* Shuze Zhu,[4] Teng Li,[2,4]† C. Alan Wright,[4] Santiago D. Solares,[2,4]† David B. Newell,[3] Nikolai B. Zhitenev,[1] Joseph A. Stroscio[1]†

We determined the electromechanical properties of a suspended graphene layer by scanning tunneling microscopy (STM) and scanning tunneling spectroscopy (STS) measurements, as well as computational simulations of the graphene-membrane mechanics and morphology. A graphene membrane was continuously deformed by controlling the competing interactions with a STM probe tip and the electric field from a back-gate electrode. The probe tip–induced deformation created a localized strain field in the graphene lattice. STS measurements on the deformed suspended graphene display an electronic spectrum completely different from that of graphene supported by a substrate. The spectrum indicates the formation of a spatially confined quantum dot, in agreement with recent predictions of confinement by strain-induced pseudomagnetic fields.

Suspending graphene sheets can remove unwanted electrical potential disturbances from supporting substrates. Initial measurements of graphene devices on SiO_2 insulating substrates achieved carrier mobilities of ≈5000 $cm^2 V^{-1} s^{-1}$ (*1*). Removing the substrate by suspending graphene resulted in mobilities in excess of 200,000 $cm^2 V^{-1} s^{-1}$ at low temperatures (*2*). These differences illustrate how substrate-induced potential disorder due to impurities and strain can play a role in the electronic properties of graphene. Recently, strain engineering of the electronic properties of graphene, which can be described through the generation of local pseudoscalar and magnetic fields by strain (*3*–*11*), has attracted considerable attention. For example,

Science

A Sharp Peak of the Zero-Temperature Penetration Depth at Optimal Composition in BaFe(As P)

K. Hashimoto, K. Cho, T. Shibauchi, S. Kasahara, Y. Mizukami, R. Katsumata, Y. Tsuruhara, T. Terashima, H. Ikeda, M. A. Tanatar, H. Kitano, N. Salovich, R. W. Giannetta, P. Walmsley, A. Carrington, R. Prozorov, and Y. Matsuda

Science, 336 (6088), • DOI: 10.1126/science.1219821

A Spike Inside the Dome

The transition temperature *T* of iron-based superconductors has a dome-shaped dependence on chemical doping, and the superconductivity that develops underneath may obscure a potential quantum critical point (QCP) residing at absolute zero. With the aim of detecting signatures of this quantum criticality, Hashimoto *et al.* (p 1554; see the Perspective by Sachdev) measured the penetration depth of the pnictide series BaFe(As P) as a function of *x*. A sharp peak right around the point where *T* has a maximum ($x = 0.30$) was observed, implying that the superfluid density diminishes sharply where one would expect it to be the most robust. This unusual finding is interpreted as a sign of a QCP at $x = 0.30$.

Science (ISSN 1095-9203) is published by the American Association for the Advancement of Science. 1200 New York Avenue NW, Washington, DC 20005. The title *Science* is a registered trademark of AAAS.